Automation in Construction 137 (2022) 104175

Contents lists available at ScienceDirect

Automation in Construction

journal homepage: www.elsevier.com/locate/autcon

Globally continuous hybrid path for extrusion-based additive manufacturing

Lingwei Xia [a], Guowei Ma [a,*], Fang Wang [b], Gang Bai [a], Yi Min Xie [c], Weiguo Xu [d], Jianzhuang Xiao [e]

[a] Smart Infrastructure Research Institute, Hebei University of Technology, Tianjin 300401, China
[b] School of Mechanical Engineering, Hebei University of Technology, Tianjin 300401, China
[c] Centre for Innovative Structures and Materials, School of Engineering, RMIT University, Melbourne 3001, Australia
[d] School of Architecture, Tsinghua University, Beijing 100084, China
[e] Department of Structural Engineering, Tongji University, Shanghai 200092, China

ARTICLE INFO

Keywords:
Extrusion-based additive manufacturing
Path planning
Global path continuity
Gap filling
Curvature optimization

ABSTRACT

In extrusion-based additive manufacturing, path filling patterns may significantly affect the printing process. To overcome printing defects incurred by path discontinuity, a Globally Continuous Hybrid Path (GCHP) is developed to solidly fill or partially fill connected domains. Discontinuous contour paths and single zigzag paths are constructed to generate locally continuous paths. These paths are subsequently connected by contour paths to render global continuity. To reduce underfilled areas without breaking path continuity, the boundaries of gap areas are evenly clipped and merged with the path. Sharp turns are optimized by fillet edges to alleviate the reduction in printing velocity. The construction results of variable shapes indicate that GCHP can continuously fill domains. The printing quality and mechanical performance of the proposed path are better than those of the previous scheme based on contour parallel paths. This study paves a new way to fabricate models using hybrid paths for extrusion-based additive manufacturing.

1. Introduction

Extrusion-based additive manufacturing, such as continuous filament fabrication [1] and 3D concrete printing [2], deposits materials layer-by-layer on a building platform to additively fabricate products. Because of the superior flexibility to produce complex geometrical shapes, these technologies have been widely applied in prototype fabrication [3], construction buildings [4], bionic structures [5], etc. The technology is a multiobjective optimization process with respect to the materials [6], printing precision [7], support optimization [8,9], stress state [10,11], etc. The tool path strategy for depositing materials is a critical factor to be considered.

All path filling schemes can be generally divided into three categories: contour parallel paths, direction parallel paths and other space filling curves. For extrusion-based fabrication, transition lines are usually exhibited during nozzle travel. Consequently, uncertainties in the extrusion amount of materials will arise at the beginning of the next tool path. To search for the shortest travel distance, solutions to the traveling salesman problem [12], ant colony optimization algorithm [13] and genetic algorithm [14] were introduced to optimize the printing path sequence. Although alleviated, the problems incurred by the breakpoints still persist. For wire and arc additive manufacturing, Ding et al. [15] discovered that insufficient metal melting at the path start led to internal defects. Additionally, to improve the mechanical performance of components printed by fused filament fabrication technology, Li et al. [16] added continuous reinforcing fibers to the matrix materials. However, automatic shear devices are required, which is usually not viable for practical installation on widespread fused filament fabrication machines. In this case, the nozzle has to be suspended to wait for continuous fibers to be clipped manually at the breakpoints before the next filament is deposited. Alternatively, commercial printers for continuous filament fabrication, such as Markforged and Anisoprint, install a shear device above the nozzle. Nevertheless, the device fails to accurately cut fibers when the fiber length is shorter than the distance of the shear device and the nozzle exit [17]. In addition, frequent clipping does not contribute well to the printing process. Based on the aforementioned deficiencies, the best solution is to fill the region by a globally connected tool path to minimize or eliminate the breakpoints along the

* Corresponding author.
E-mail address: guowei.ma@hebut.edu.cn (G. Ma).

https://doi.org/10.1016/j.autcon.2022.104175
Received 10 June 2021; Received in revised form 10 January 2022; Accepted 13 February 2022
Available online 10 March 2022
0926-5805/© 2022 Elsevier B.V. All rights reserved.

path.

When the width of the area to be filled is smaller than the nozzle diameter, the area is usually not included in the deposition procedure [18]. Consequently, underfilled gaps occur. Additionally, as one of the directional parallel paths, the zigzag path is a prevailing infill pattern because of its simplicity and ease of implementation. However, sharp corners exist in the paths and incur printing steps, which affects fabrication accuracy [19]. Inevitable deceleration and acceleration of nozzle movement are exhibited at sharp corners [20]. Ma et al. [21] also discovered that when printing concrete with continuous microcable fibers, the fibers are apt to be pulled out from matrix materials at sharp corners because of their different stiffnesses and weak interface bonding between the slurry and the fibers. In contrast, these situations are greatly improved when printing low-curvature filling curves.

The hybrid path, which consists of zigzag paths and contour paths, is the most widely employed printing strategy by extrusion-based additive manufacturing. In this study, a novel path scheme is proposed to continuously fill the connected geometries. The novelties of the current study can be stated as follows:

- The global continuity of hybrid path is implemented, aims to eliminate negative effects caused by path breakpoints.
- A partial infill strategy of a globally continuous path is implemented to save printing materials and time expenses.
- A gap filling method is proposed to solidly fill the printing void whose width is smaller than the nozzle diameter.
- An adaptive curvature optimization strategy is developed to alleviate the velocity deceleration due to sharp corners.
- Samples printed by the proposed Globally Continuous Hybrid Path (GCHP) demonstrate higher mechanical properties and fabrication qualities than those printed by the previous continuous path.

The remainder of the manuscript is organized as follows: In Section 2, relevant research works are reviewed. In Section 3, the methodologies for GCHP, including path continuity, gap filling and curvature optimization, are explained in detail. In Section 4, variable complexity shapes filled by the GCHP and the corresponding computational expenses are presented. Comparisons for variable paths with respect to filling ratio, printing quality, fabrication expense and mechanical performance are conducted. Conclusions and future works are presented in Section 5.

2. Related works

2.1. Path continuity

Based on the contour path, a Connected Fermat Spiral (CFS) tool path was proposed to generate long and low-curvature paths [22]. However, this scheme does not guarantee true space filling and is not suitable for filling porous structures. To make amendments, Zhai and Chen [23] decomposed geometries by the Voronoi algorithm and then constructed a continuous path by connecting Fermat spiral curves in the merged subregions. The printing quality by this methodology is considerable, but the ultimate strength of printed structures with these paths is lower than that of their counterparts with direction parallel paths, because orientations of the contour parallel paths cannot be waved crosswise and adjusted to strengthen the mechanical performance of the printing products. Partial infill, a common strategy to save material consumption and printing time, is widely used in extrusion-based additive manufacturing. Unfortunately, partial infill of contour parallel paths results in filaments isolated from each other due to lack of connection of adjacency paths. These properties negate the popularity and applicability of the above methodologies.

Researchers have also endeavored to improve the path continuity of direction parallel paths. Dwivedi and Kovacevic [24] proposed an automated torch path planning methodology by connecting offset zigzag paths in decomposed monotonous polygons. Nevertheless, the printing step incurred by the corners negates surface precision, and the decomposition method is not viable for hollow structures. Referencing the hybrid and adaptive path generation approach [25], Jin et al. [26] inputted two outer contours in the non-retraction path to cover the printing steps and improved the strategy to decompose the geometry with inner hollowness. However, this scheme does not fulfill the global continuity of interior directional parallel paths and contour paths of inner holes. For the geometry that comprises several fill regions divided by contours, this scheme is not applicable. Ding et al. [15] proposed an optimal path generation scheme for wire and arc additive manufacturing. Similarly, all geometric decomposition strategies are only suitable for simple polygons rather than complicated porous structures with consecutive concave angles and smooth boundaries. Schemes of the prevailing continuous direction parallel paths are either restricted by geometric complexity or incompletely continuous [22].

2.2. Method to fill void

Jin et al. [27] decomposed geometries into monotone polygons, and scanning widths of direction parallel paths were then adaptively adjusted to fill the subregions to sufficiently fill the printing area. Similarly, the decomposition scheme is restricted by the geometric complexity of the inner holes. For contour parallel paths, Jin et al. [28] adaptively adjusted the point locations of the path to locally optimize the path spacing. Although the gaps are evenly distributed between adjacent paths, the gaps are still exhibited. Ding et al. [29] proposed a practical path, which fills the region by paths that offset axle wire from the inner to the outer boundaries. Xu et al. [30] developed a variable-size square nozzle and corresponding adaptive path planning method. These methods significantly reduce the underfilled gaps. Additionally, the fill gap function was developed in open-source software such as Cura [31] and Slic3r [32], but severely discontinuous short paths generated by this method are exclusively applicable for manufacturing techniques using thermoplastic materials.

2.3. Smoothing optimization

Jin et al. [33,34] introduced non-uniform-rational-B-spline-based curves in path planning to improve the surface accuracy and printing efficiency. Subsequently, a spline parameter curve was introduced to connect discontinuous zigzag paths [20]. The ends of the spline and zigzag path are set as tangency; thus, the velocity deceleration is avoided when the end point of the zigzag path traverses to the start point of nozzle travel. The most commonly adopted method to smoothen corners in continuous contour parallel paths is the Laplacian method using the iterative Gauss-Newton method [22]. Giberty et al. [35] employed the Bezier curve to smoothen corners to enable the nozzle to move steadily along the tool path despite slight oscillations. However, the computational expense of these methodologies with a complex calculation process is not satisfactory.

3. Methodology

In this section, the computational procedures of the GCHP, which fills a connected region by a closed loop path, are introduced. To remove the restriction by boundary complexity, geometric decomposition is intelligently circumvented when constructing zigzag paths. Path continuity is comprised of two steps by the depth-first search algorithm. As contour paths, discontinuous double zigzag paths are connected to closed loops to fulfill local continuity. These paths are then connected by contour paths based on their connectable relationships to implement global continuity. The gap areas are filled by crossed zigzag paths perpendicular to the original path orientation, and sharp corners are optimized by adaptive fillet edges using a vectorized algorithm. All the calculation is implemented in Matlab. The Boolean operation for geometry computation is implemented by an open-source graphic library

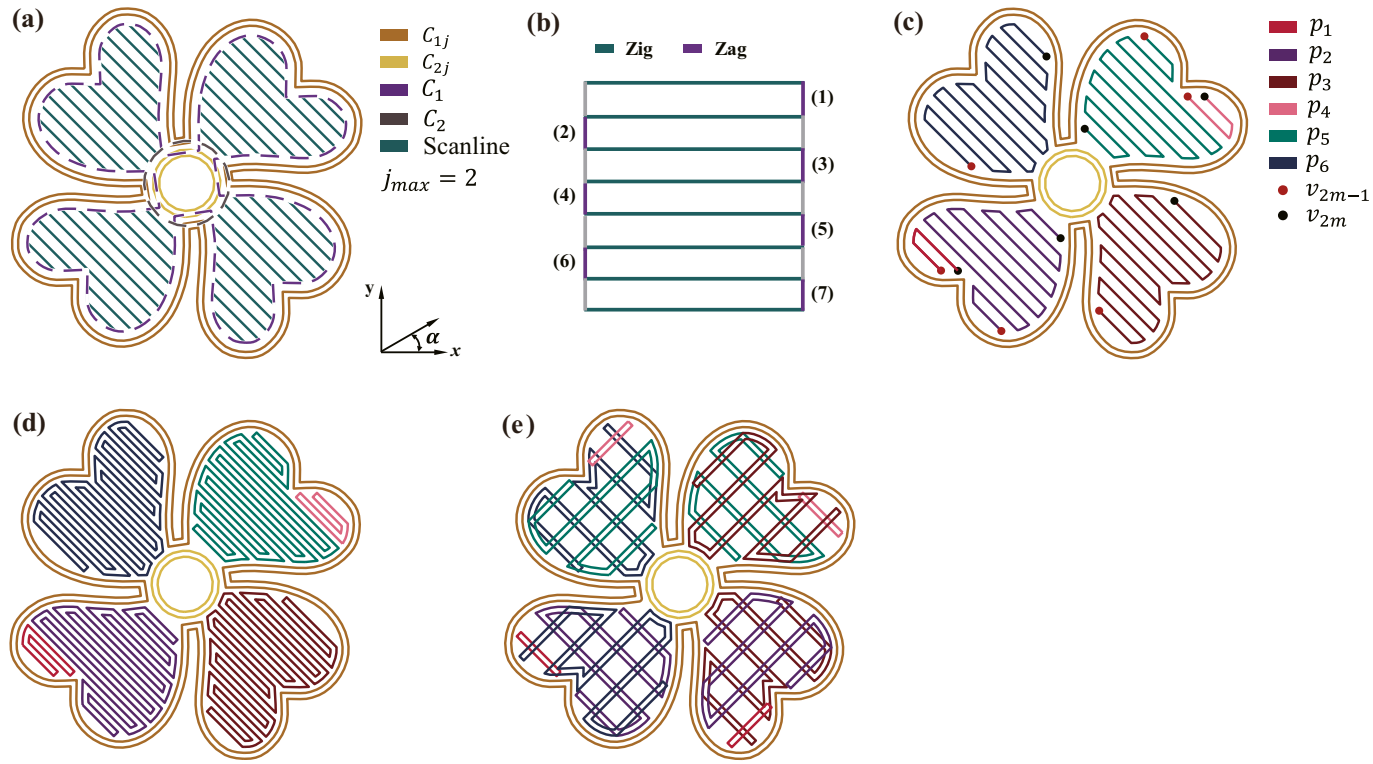

Fig. 1. Schematic of the generation of discontinuous hybrid path for one layer: (a) contour and scanline generation ($\alpha = -\pi/4$); (b) connection of zigs and zags based on even-odd rule; (c) discontinuous single zigzag paths (v_{2m-1} and v_{2m} indicate the start points and end points of path p_m, respectively); construction results of discontinuous hybrid path with (d) solid infill; and (e) partial infill.

in MathWorks [36].

3.1. Discontinuous hybrid path

Fig. 1 presents a schematic of generating a discontinuous hybrid path for one layer. As shown in Fig. 1(a), boundaries are offset inwards at an interval of $(j - 0.5) \times d$ to generate contour paths C_{ij}, where i indicates the boundary number, j represents the layer number of contours, and d is the nozzle diameter. Discontinuous single zigzag paths are generated to serve as references to construct discontinuous double zigzag paths. For solid infill, parallel scanlines are generated based on the preset angle α and double nozzle diameter $2d$. Geometric boundaries offset $(j_{max} + 1)d - d_{in}$ inwards the filling area to generate C_i to clip and connect scanline segments, where d_{in} indicates the insert distance of interior paths and contour paths. As indicated in Fig. 1(b), scanlines (zigs) and partitioned C_i (zags) are connected based on the even-odd rule. In the direction perpendicular to α, the unvisited outermost (top) zig path is chosen as the origin. The scanlines are traversed to the opposite side (bottom), and zag paths with even and odd numbers are added to the right and to the left, respectively, to connect the zig paths. These procedures are repeated until all the scanlines are connected to form discontinuous single zigzag paths p_m, as shown in Fig. 1(c), where the distance of contour paths is d and the distance of direction parallel paths is $2d$. Zigzag paths are then offset $0.5d$ inwards and outwards to generate discontinuous double zigzag paths P_m. Partial infill adopts a crosswise waved pattern with orientations of α and $\alpha + \pi/2$ in one layer, and the distance of scanlines is $4d/w$, where w represents the filling ratio. The construction results for discontinuous hybrid paths with solid infill and partial infill are shown in Figs. 1(d) and 1(e), respectively. Except for the distance of outer zag paths and its closest contour path is $d - d_{in}$, the path distance of solid infill strategy is d, and the path distances of partial infill are d and $(4d/w - d)$.

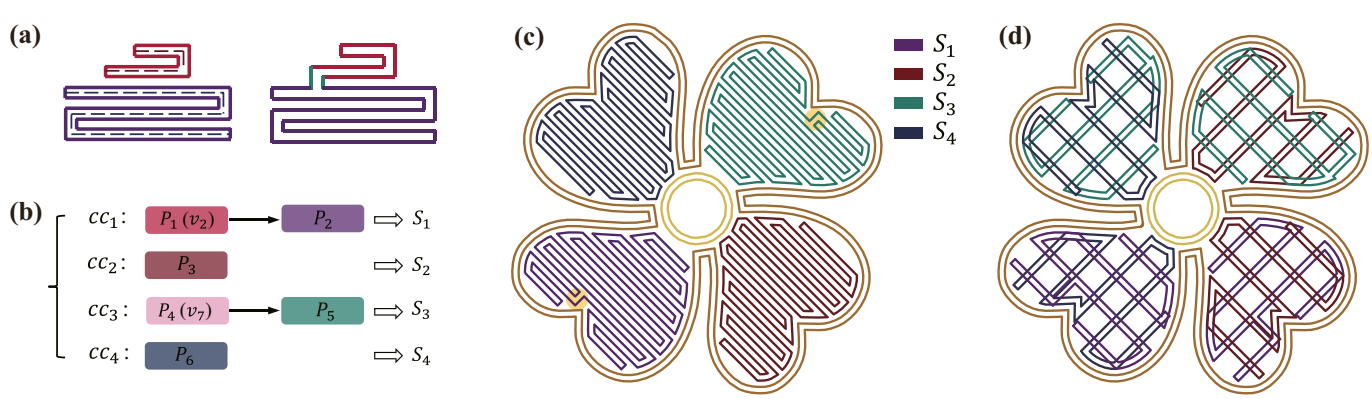

Fig. 2. Schematic of the local continuity: (a) connection method for connecting double zigzag paths; (b) connected components ($P_1(v_2) \rightarrow P_2$ denotes that the end of path P_1, v_2, is connectable to P_2); locally continuous hybrid path for (c) solid infill; and (d) partial infill.

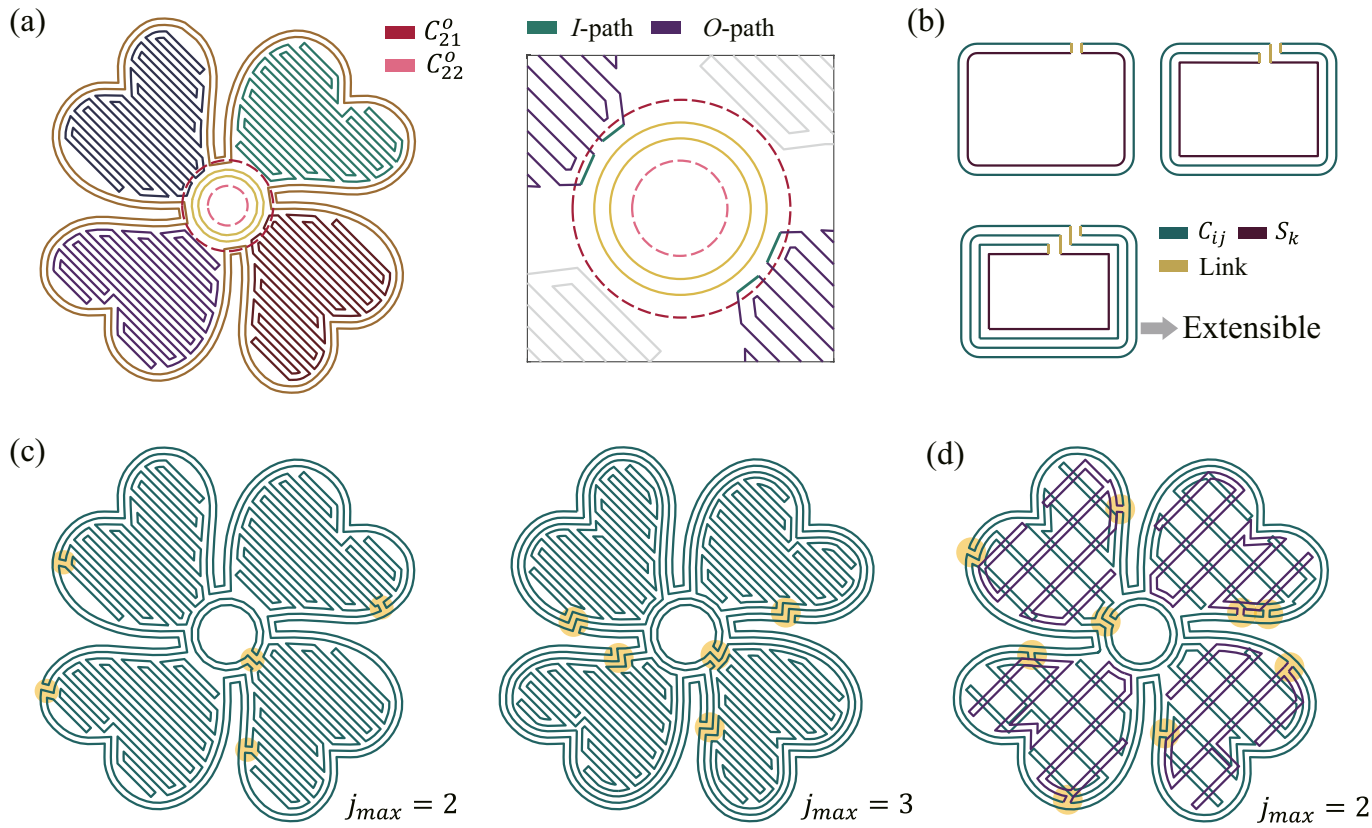

Fig. 3. Schematic of the global continuity: (a) reference geometries (dotted line) and illustration of the *I*-path and *O*-path; (b) connection methods of the double zigzag and contour paths; construction results for (c) solid infill GCHP with two and three contours; and (d) partial infill GCHP with two contours.

3.2. Path continuity

3.2.1. Local continuity

Fig. 2 shows a schematic for the fulfillment of local continuity. Notably, in the solid infill strategy, if the shortest vertical distance between an endpoint and an edge of another single zigzag path is $2d$, then the corresponding double paths can be connected by a link, as shown in Fig. 2(a). The connectable relationships for all the interior double zigzag paths are then counted to construct the directed graph $G\left(V, \vec{E}\right)$, where $V = \{v_1, v_2, \cdots, v_{2m-1}, v_{2m}\}$ denotes endpoints of reference paths and $\vec{E} = \{\vec{e_1}, \vec{e_2}, \cdots, \vec{e_n}\}$ represents directed connectable relationships. The relationships are expressed in an adjacency matrix A, where elements $a_{i'j'}$ are expressed as

$$a_{i'j'} = \begin{cases} 1 & P_{[i'/2]} \text{ end } v_{i'} \text{ is connectable to } P_{j'} \\ 0 & \text{otherwise} \end{cases} \tag{1}$$

As shown in Fig. 2(b), an arbitrary unvisited double zigzag path is specified as the start path S_k, and a corresponding connected component cc_k is built. By introducing a depth-first search algorithm, the matrix A is traversed to identify an unvisited path that is connectable to paths in cc_k. Subsequently, the connectable path is stored in cc_k and merged with S_k. This process is repeated until no path is connectable to the latest S_k. The next connected components are then constructed until no double zigzag paths are connectable to each other. The difference of the partial infill strategy is that the latter needs to separately construct locally continuous paths with orientations of α and $\alpha + \pi/2$, and the shortest vertical distance to search connectable adjacency paths is $4d/w$. Locally continuous paths of the solid and partial infill strategies are shown in

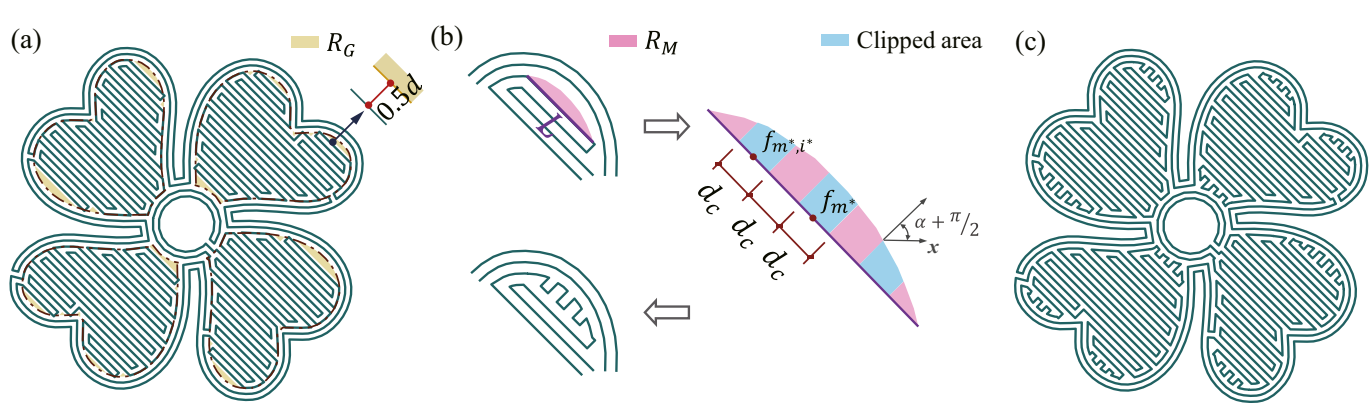

Fig. 4. Schematic of gap filling: (a) underfilled gaps; (b) method of filling gaps; (c) construction result.

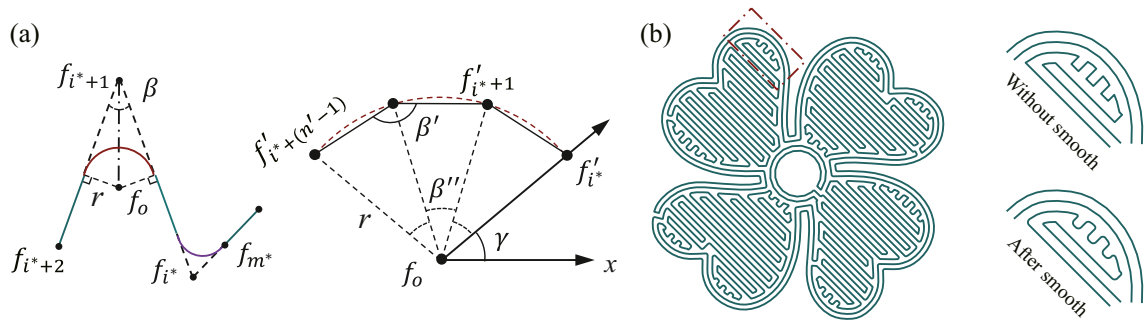

Fig. 5. Schematic of the curvature optimization: (a) transition arcs; (b) construction result.

Fig. 2(c) and (d), respectively.

3.2.2. Global continuity

Fig. 3 shows a schematic for rendering global continuity. Geometric boundaries are offset $\pm d^o((j_{max}+0.5)d - d_{in} < d^o < (j_{max}+1.5)d - d_{in})$ to generate reference geometries $C_{i1}{}^o$ (offset outwards) and $C_{i2}{}^o$ (offset inwards), as indicated by the dotted line in Fig. 3(a). If a reference intersects with a locally continuous path, then this path is specified as connectable to corresponding contours. The connectable relationships of C_{ij} and S_k are counted. In this calculation, paths S_1, S_2, S_3 and S_4 are connectable to C_{1j}, and paths S_2 and S_4 are connectable to C_{2j}. Every connectable path is divided into two parts by the reference geometries, i.e., path edges that are located inside (*I*-path) and outside (*O*-path) the reference. For $C_{i1}{}^o$ and $C_{i2}{}^o$, comparatively smooth *I*-paths and *O*-paths, respectively, are selected to be broken and reconnected to the corresponding contours. The choice of the connection method shown in Fig. 3(b) relies on the number of closed loops. The connection sequence of loops is specified from the interior to the exterior since connection positions that are improperly located possibly fail the connection if there are limited applicable *I*- or *O*-paths. All the contours and interior paths are connected in sequence until global continuity is achieved. For the example shown in Fig. 3(a), paths S_1 and C_{1j} are merged by the connection method of three loops. S_2, S_3 and S_4 are then merged to the new path by the connection method of two loops. After the connection of C_{2j} and the latest path by the connection method of three loops, the calculation ends. Fig. 3(c) and (d) show the construction results for globally continuous paths using the solid infill and partial infill strategies, respectively.

3.3. Gap filling

Fig. 4 presents a schematic for the gap filling procedure, which is developed for domains that need to be solidly filled. This step processes gaps with filling widths smaller than the nozzle diameter, as well as large gaps incurred by sharp corners. The solid plane domain R_P, which is translated from the continuous path, is offset inwards and outwards $0.5d$ to generate the path printing area $R_P{}^o$. And geometric boundaries are offset $(j_{max}+0.5)d - d_{in}$ inwards to construct area R_S, whose boundary (the dotted line in Fig. 4(a)) represents the idealized boundary for the internal direction parallel paths to implement full filling. Consequently, the underfilled area R_G in R_S can be calculated as

$$R_G = R_S - R_P^o \tag{2}$$

where R_G is indicated by the yellow region in Fig. 4(a). R_G is separated from R_P, and the distance between their parallel boundaries is $0.5d$. To calculate the appropriate area R_M to merge with R_P, R_G is offset outwards $0.5d$ to generate $R_G{}^o$. It is worth noting that the boundary distance between $R_G{}^o$ and the innermost contour path is $0.5d$, which will generate overfilled areas if paths go along with these two boundaries. Thus, $R_G{}^o$ should subtract this redundancy part that locates outside R_S. R_M can be expressed as

$$R_M = R_G^o \cap R_S \tag{3}$$

As the pink area shown in Fig. 4(b), R_M locates at distance d away from the innermost contours and shares a common edge L (purple color) with R_P. Employing a rounding method, path planning of R_M is divided into the following three categories according to the length of L. If the length of the common edge $L > 2d$, R_M is clipped evenly by rectangles with a width of d_c and then merged with R_P. d_c is calculated as

$$d_c = \frac{L}{Round(L/d)} \tag{4}$$

The midpoint coordinates f_{m^*,i^*} of rectangular edges that belong to L are expressed by

$$\begin{aligned} &[x_{m^*,i^*}, y_{m^*,i^*}] = [x_m, y_m] \pm i^* \cdot d_c \cdot [cos\alpha, sin\alpha] \\ &\begin{cases} 0 \le i^* \le \lceil \frac{L}{4d_c} - 1 \rceil & \lceil \frac{L}{2d_c} - 1 \rceil \text{is odd} \\ 1 \le i^* \le \lceil \frac{L}{4d_c} - 1 \rceil & \lceil \frac{L}{2d_c} - 1 \rceil \text{is even} \end{cases} \end{aligned} \tag{5}$$

where $[x_m, y_m]$ represents the midpoint location of L. If $d \le L < 2d$, R_M is directly merged with R_P. Otherwise, R_M is not included in the calculation process. The construction result is shown in Fig. 4(c).

3.4. Curvature optimization

Fig. 5 shows the schematic of curvature optimization. With reference to Zhao et al. [22] and Zhai et al. [23], the angle of the sharp corner is specified as 0.6π. If the path angle β is smaller than 0.6π, the sharp corner is substituted by a tangent transition arc, as indicated by the red arc in Fig. 5(a). The fillet radius of arcs is specified as r. To optimize all the sharp corners and guarantee a sufficient transferred length of the next edge to accommodate the arc, r is adjusted to

$$r = \left(\frac{\overline{f_{i^*} f_{i^*+1}} tan(\beta/2)}{2}, \frac{\overline{f_{i^*+1} f_{i^*+2}} tan(\beta/2)}{2} \right)_{min} \tag{6}$$

in the circumstance that the minimum half length of adjacency edges of β is shorter than the above values, such as the purple arc in Fig. 5(a). Because stepper motors move in straight lines, the arc is approximately approached by fillet edges. To prevent tiny edges from restricting the printing speed, the number of insertion points n' should be limited as long as the angle value β' of adjacency edges is larger than 0.6π. n' is calculated as

$$\left(\begin{aligned} \beta' &= \frac{\pi \cdot (n'-1) - (\pi - \beta)}{n'-1} \\ \beta' &> 0.6\pi \end{aligned} \right. \quad \Rightarrow \quad n' = \lceil \frac{\pi - \beta}{0.4\pi} + 1 \rceil \tag{7}$$

The coordinates of insertion points $f_{i^*+j^{*\prime}}$ are expressed by

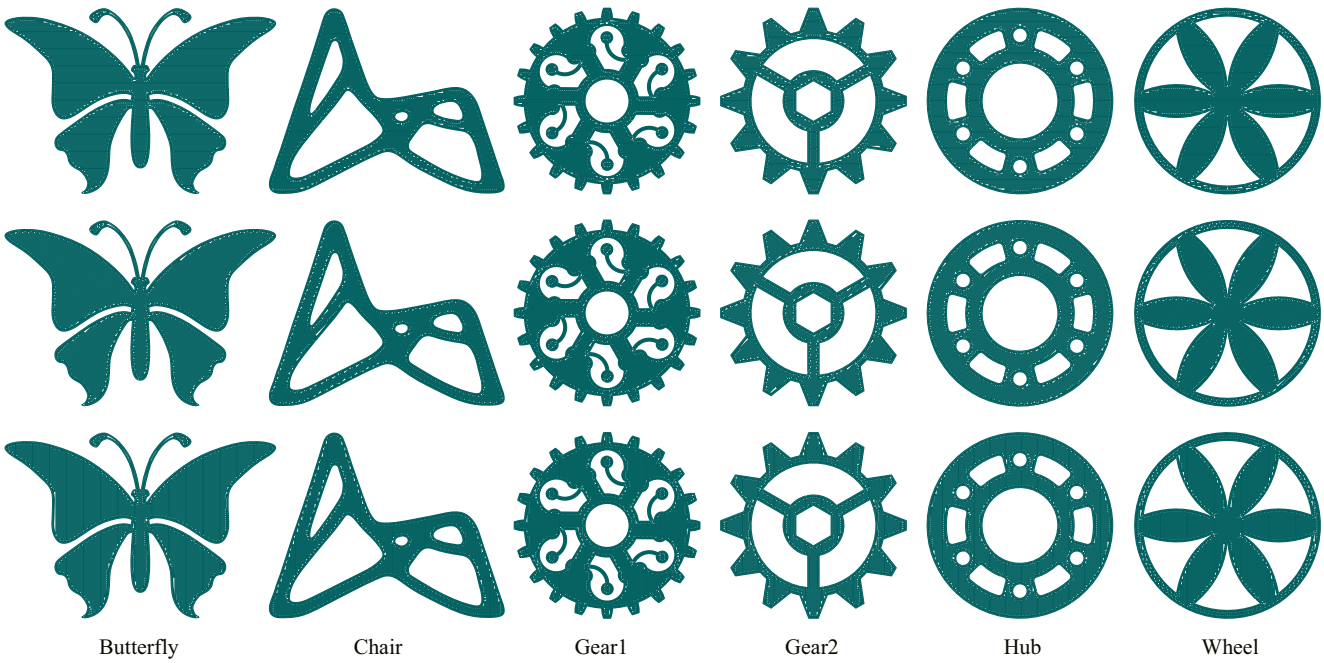

Fig. 6. Models and corresponding solid infill GCHPs ($d = 0.4\ mm$, $d_{in} = 0.12\ mm$, $r = 0.1\ mm$).

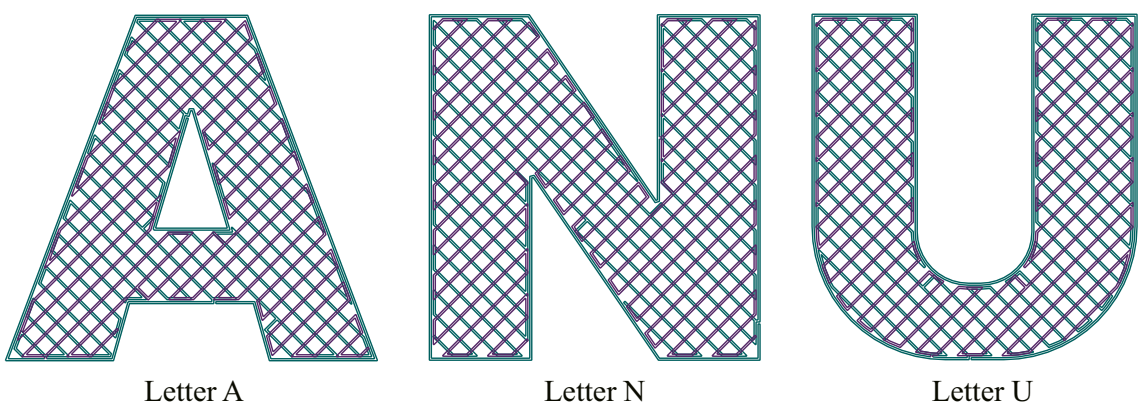

Fig. 7. Models and corresponding partial infill GCHPs ($d = 0.4\ mm$, $d_{in} = 0\ mm$, $r = 0.1\ mm$, w=0.5).

$$[x_o y_o] = [x_{i^*} y_{i^*}] + r \cdot csc(\beta/2) \cdot \overrightarrow{(f_{i^*+1} f_o)}_0 \tag{8}$$

$$\beta^{'} = \frac{\pi - \beta}{n^{'} - 1} \tag{9}$$

Table 1
Peak Memory (PM) and Computational Time (CT) of contour path (Con), CFS, zigzag path (Zig), and global continuity ($Step_{con}$), gap filling ($Step_{gap}$) and curvature optimization ($Step_{opt}$) of the GCHP during calculation.

Factor	Con	CFS		Zig			GCHP					
Path							$Step_{con}$		$Step_{gap}$		$Step_{opt}$	
Expense	PM (*Kb*)	CT (*s*)	PM (*Kb*)	CT (*s*)	PM (*Kb*)	CT (*s*)	PM (*Kb*)	CT (*s*)	PM (*Kb*)	CT (*s*)	PM (*Kb*)	CT (*s*)
Butterfly	1472	0.87	18,360	5.24	676	0.79	3560	3.98	1576	3.35	1024	0.29
Chair	2240	1.00	8876	3.48	1358	0.31	2036	1.80	4340	2.94	2220	0.20
Gear1	1452	0.94	9048	8.65	896	1.69	2092	6.23	4832	13.46	712	0.48
Gear2	1464	0.91	2608	3.79	1366	0.62	4696	1.84	5148	3.27	1580	0.18
Hub	2908	0.99	28,976	15.00	860	0.60	1084	3.06	1836	3.23	792	0.21
Wheel	1332	0.93	3888	3.00	1024	0.59	1308	2.20	7772	4.38	920	0.22
Letter A	–	–	–	–	–	–	552	1.30	–	–	1032	0.30
Letter B	–	–	–	–	–	–	632	1.18	–	–	1028	0.34
Letter C	–	–	–	–	–	–	680	1.62	–	–	1032	0.30

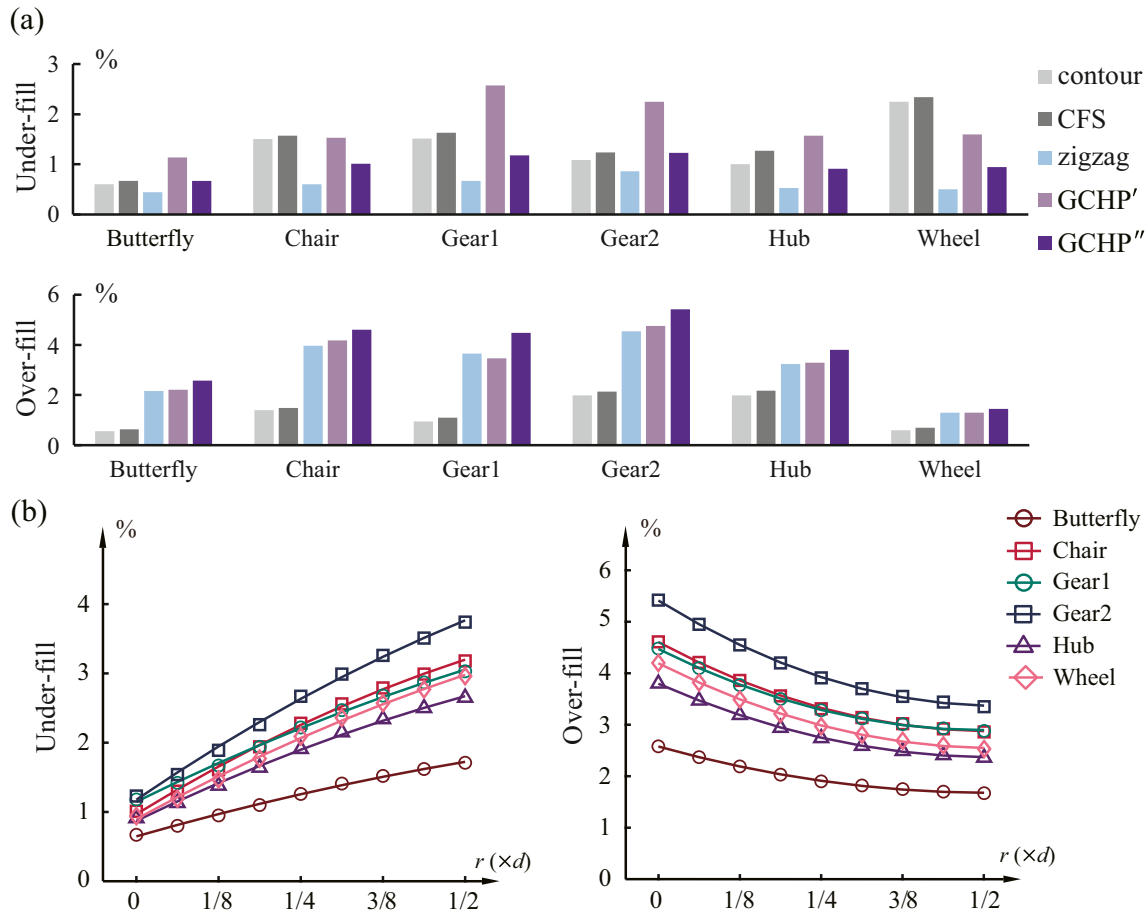

Fig. 8. Filling ratios for (a) variable paths (GCHP' and GCHP'' are GCHP before gap filling and GCHP before curvature optimization, respectively) and (b) GCHP against the variable fillet radii during curvature optimization.

$$\begin{cases} f_{i^*} \text{ to } f_{i^*+(n'-1)} \text{ is anticlockwise :} \\ \left[x_{i^*+j^*}', y_{i^*+j^*}'\right] = [x_o, y_o] + r\cdot[cos(\gamma + j^*\cdot\beta^{''}), sin(\gamma + j^*\cdot\beta^{''})],\ j^*\varepsilon[0, n'-1] \\ f_{i^*} \text{ to } f_{i^*+(n'-1)} \text{ is clockwise :} \\ \left[x_{i^*+j^*}', y_{i^*+j^*}'\right] = [x_o, y_o] + r\cdot[cos(\gamma - j^*\cdot\beta^{''}), sin(\gamma - j^*\cdot\beta^{''})],\ j^*\varepsilon[0, n'-1] \end{cases} \tag{10}$$

where $[x_o, y_o]$ indicates the center coordinate f_o of the arc, $\overrightarrow{(f_{i^*+1}f_o)}_0$ denotes the unit vector from points $f_i{}^*{}_{+1}$ to f_o, and γ represents the angle between the vector $\overrightarrow{f_o f_{i^*}'}$ and the x-axis. The curvature optimization result is shown in Fig. 5(b).

4. Experimental results and discussion

To demonstrate the versatility of the proposed path, geometries containing variable exterior and interior complex boundaries and holes filled by solid and partial infill GCHPs are exemplified in Fig. 6 and Fig. 7, respectively. These shapes are comprehensively representative of potential intricacies, such as path discontinuities, sharp corners and underfilled gaps, in path planning. The peak memory and computational time of the contour path, CFS, zigzag path and three steps (i.e., global continuity, gap filling and curvature optimization) of GCHP are reported in Table 1. In this section, all the zigzag paths and solid infill GCHP data represent average values of four layers ($\alpha = 0, \pm\pi/4, \pi/2$). Procedure quantities are monitored on a laptop equipped with an Intel (R) Core (TM) i7-7700HQ CPU 2.80 GHz with 16 GB RAM. The peak memory and computation time of CFS are the highest. Because contour parallel paths consist of abundant points, the postprocessing of these points to implement continuity requires higher calculation expenses than GCHP. Memory consumption of the novel scheme is not substantial, which does not particularly increase with the ongoing calculation because most data of the previous layers are cleared when constructing the following layers. Running time is mainly spent on the steps of global continuity and gap filling, and it will be linearly increased with the calculation of increment layers.

4.1. Filling ratio of solid infill strategy

The filling ratios of the contour path, CFS, zigzag path with two contours and the proposed path are shown in Fig. 8. Except for the GCHP, the other three paths are generated by Cura. It is not feasible to accurately measure the filling ratio of the printed models. By default, tool paths are set with a nozzle width to theoretically evaluate the underfilled and overfilled areas. As shown in Fig. 8(a), the underfilled ratio of GCHP' (GCHP without gap filling and curvature optimization) is severe because its initial nozzle width is 2*d*. As expected, the gap filling procedure significantly reduces underfilled areas without breaking path continuity. In contrast, curvature optimization tends to increase underfilled areas but reduce overfilled areas near sharp corners, as shown in Fig. 8(b). The smoother the corner is, the lower the overfilled areas will be and the larger the underfilled areas will be. The overfilled ratio of GCHP is the most substantial, which is mainly incurred by the overlap of outer zag paths and contour paths. It should be noted that overlap is not the dominant factor in reducing printing quality, since overfilled materials are usually flattened by the nozzle and the printing result is also affected by other printing imprecisions.

Table 2
Path numbers (N_{path}), travel (L_{travel}) and path (L_{path}) length, material consumption (*Mat*), printing time (*Time*) and effective speed ($\overline{V}$) for contour (Con) path, CFS, zigzag (Zig) path and GCHP'' (GCHP'' is GCHP before curvature optimization).

Factor	N_{path}				L_{travel} (*mm*)				L_{path} (*mm*)			
Input	Con	CFS	Zig	GCHP''	Con	CFS	Zig	GCHP''	Con	CFS	Zig	GCHP''
Butter	101	1	18	1	375	0	419	0	8052	8052	8194	8210
Chair	80	1	22	1	278	0	321	0	4756	4757	4922	4933
Gear1	140	1	59	1	589	0	919	0	6589	6592	6825	6846
Gear2	121	1	25	1	283	0	407	0	4356	4356	4477	4498
Hub	142	1	46	1	361	0	520	0	6560	6554	6672	6683
Wheel	96	1	25	1	211	0	499	0	6516	6517	6836	6854

Factor	*Mat* (*mm*)				*Time* (*s*)				$\overline{V}$ (*mm/s*)			
Input	Con	CFS	Zig	GCHP''	Con	CFS	Zig	GCHP''	Con	CFS	Zig	GCHP''
Butter	267.8	267.8	272.6	273.1	181	176	194	184	44.5	45.8	42.2	44.5
Chair	158.2	158.2	163.7	164.1	107	106	118	120	44.4	44.8	41.6	41.1
Gear1	219.2	219.2	227.0	227.7	172	165	184	176	38.2	40.0	37.1	38.8
Gear2	144.9	144.9	148.9	149.6	108	109	116	115	40.3	40.0	38.7	38.9
Hub	218.2	218.0	221.9	222.3	149	147	160	160	44.0	44.6	41.6	41.6
Wheel	216.7	216.8	227.4	228.0	156	155	177	165	41.8	42.0	38.6	41.6

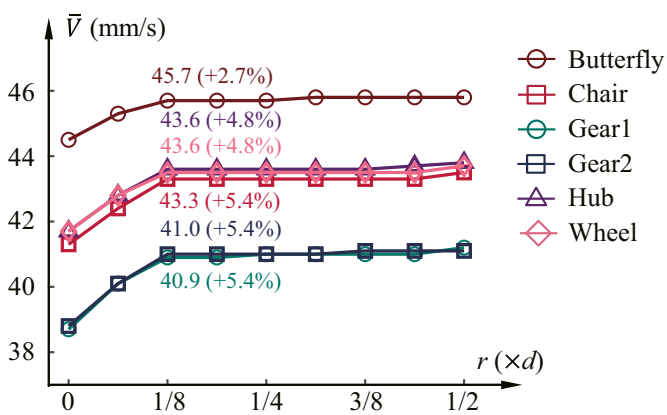

Fig. 9. Effective velocity of the GCHP against variable fillet radii during curvature optimization.

4.2. Fabrication expense

The corresponding fabrication expenses with variable filling schemes are listed in Table 2. Using a 1.75 *mm* diameter thermoplastic polylactic acid filament (density: 1.28 gcm^{-3}, glass transition temperature: 60 °C, Suzhou Kexcelled Co., Ltd.), all the samples in Fig. 6 with variable paths are fabricated by a Delta desktop printer with a 0.4 *mm* nozzle. Each layer is set to a thickness of 0.2 *mm*, and the filling speed is 50 *mm/s*. The retraction speed and distance are set to 30 *mm/s* and 3 *mm*, respectively. As shown in Table 2, CFS and GCHP'' (GCHP before curvature optimization) only generate one continuous path with no nozzle travel for connected domains. A larger path number and longer travel length imply that more printing errors can be incurred during the printing process. Path lengths of the contour path and CFS are shorter than direction parallel paths, which implies less material and time expenses. However, less material consumption may incur more underfilled gaps, which will be discussed in the next subsection. Because the real printing time is affected by the total travel and path lengths, the effective velocity is calculated as

$$\overline{V} = \frac{L_{path}}{Time} \; mm \Big/ s \tag{11}$$

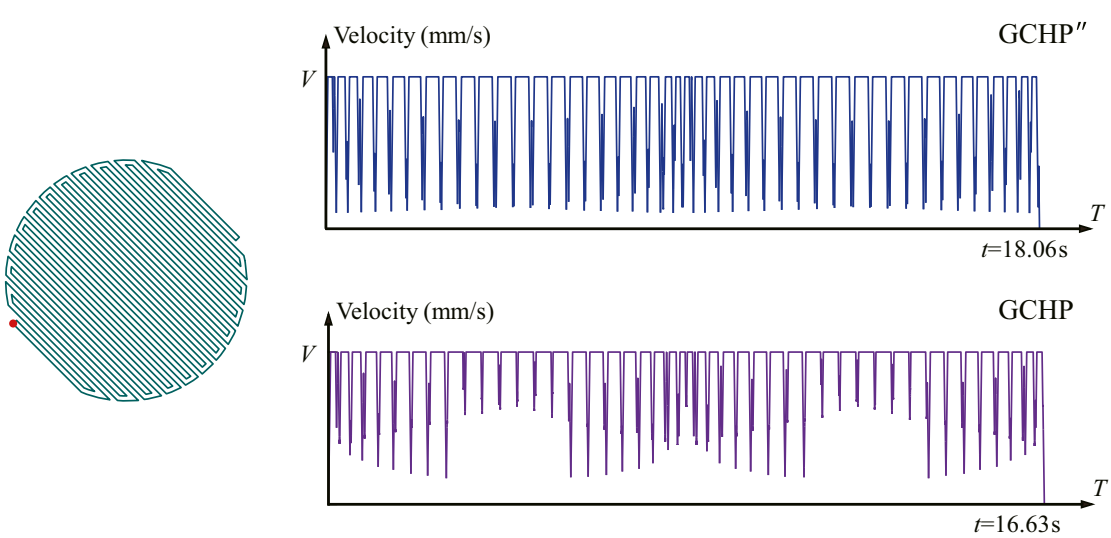

Fig. 10. Velocity of path before (GCHP'') and after (GCHP) curvature optimization.

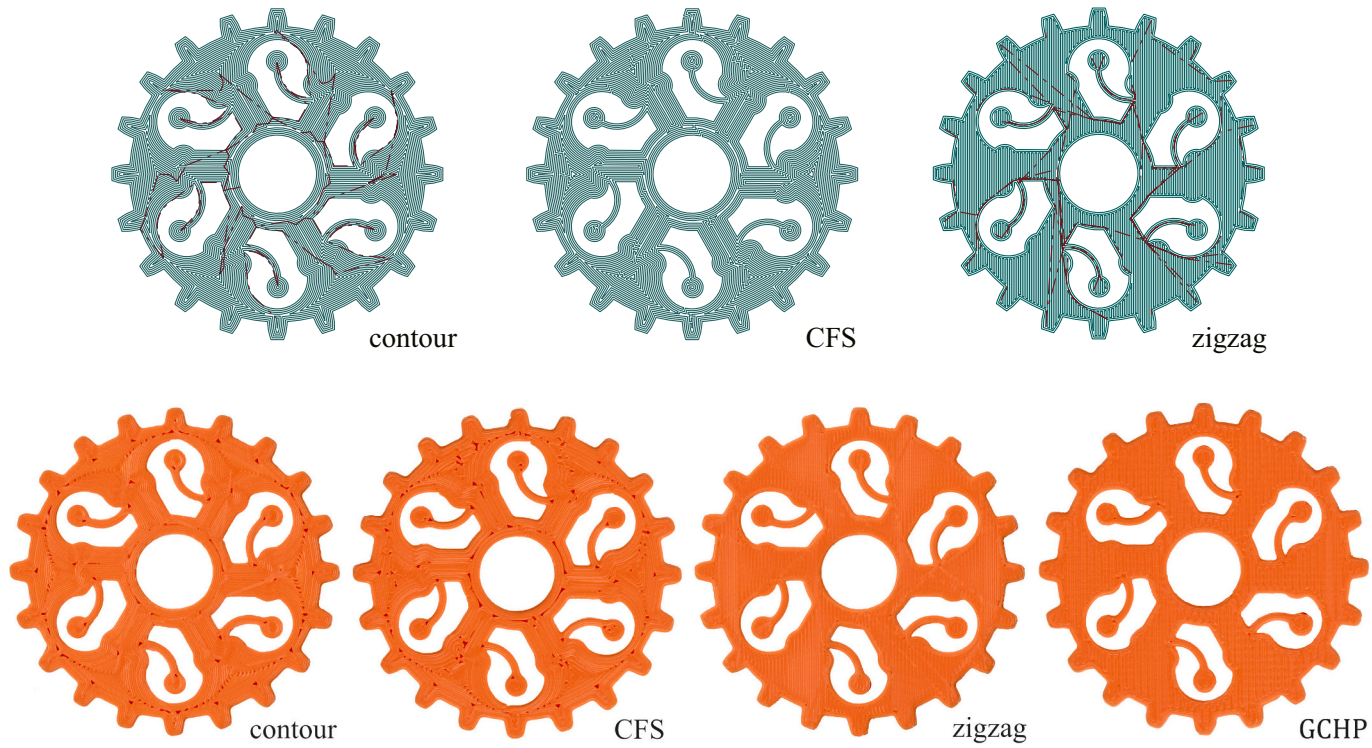

Fig. 11. Printing results for variable paths with the solid infill strategy (red dotted lines represent trajectories of nozzle travel). (For interpretation of the references to color in this figure legend, the reader is referred to the web version of this article.)

Generally, $\overline{V}$ of the zigzag path and GCHP'' is slower than that of their counterparts because more number of sharp turns increase the velocity reduction, which is an inherent defect of the former. Curvature optimization is conducted based on these findings. $\overline{V}$ for the GCHP against the variable fillet radii is illustrated in Fig. 9. $\overline{V}$ is significantly improved when $r \leq d/8$. The improved $\overline{V}$ surpasses that of the traditional zigzag path and compares favorably with CFS. In contrast, the limited change in $\overline{V}$ when $r > d/8$, which can be attributed to that the velocity of the current point is also restricted by the lengths of edges and the velocities of other points. A linear velocity model [37] is established to exposit the improvement, as shown in Fig. 10. The corresponding parameters are set based on our machine with an expected velocity $V = 50\ mm/s$, and acceleration $A = 1000\ mm/s^2$, and sampling period $T_s = 0.01\ s$. Curvature optimization alleviates the reduction in velocity incurred by sharp corners, thus saving printing time.

4.3. Printing quality

Sample Gear1 fabricated by variable paths is presented in Fig. 11 to compare their fabrication quality. Because $\overline{V}$ is invariant when $r > d/8$, whereas the underfilled gaps are still increased with the increment of fillet radii, r is tentatively set to the threshold value $d/8$. As shown in Fig. 11, for traditional zigzag and contour paths, materials suspended in the nozzle are consumed during nozzle travel, which incurs conspicuous transition lines. This phenomenon can be alleviated by the retraction function but cannot be thoroughly eliminated. The first step of constructing contour parallel paths is to decompose the domain into a set of subregions, each of which is filled with closed contour paths that are offset by boundaries. Underfilled gaps, which occur at the adjacency of subregions and corners, are serious in contour path and CFS. In contrast, generating slight overfilled areas, gaps near geometric boundaries in the zigzag path and GCHP are alleviated or even eliminated by inserting interior paths into contour paths. As a result, the proposed path exhibits better printing quality than CFS because of less visible large underfilled gaps. The printing result of the letter model N with partial infill GCHP is shown in Fig. 12, which cannot be implemented by CFS because of separated contour paths.

Fig. 12. Printing results for GCHP with the partial infill strategy.

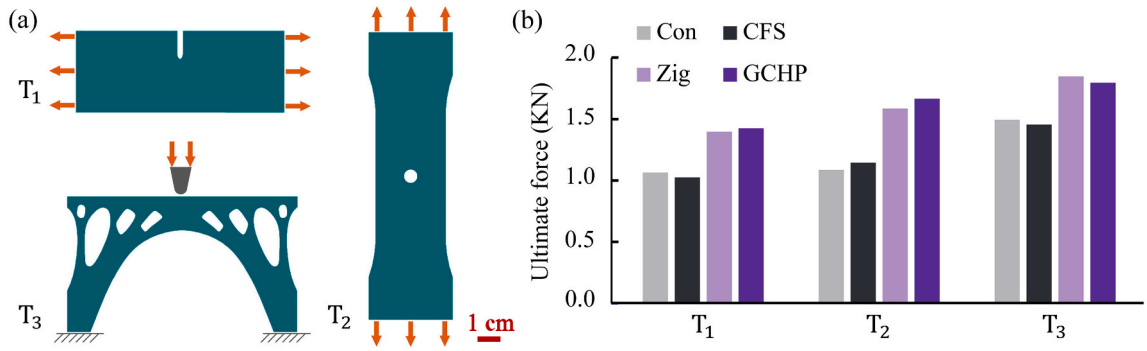

Fig. 13. Mechanical tests: (a) models and load conditions; (b) ultimate force of specimens for contour (Con) path, CFS, zigzag (Zig) path and GCHP.

4.4. Mechanical performance

The mechanical performance of the printing products mainly depends on the connection and strength per se of the filaments. As shown in Fig. 13(a), three models are designed and fabricated by variable paths to compare their ultimate load-bearing capacities. The printing material is the polylactic acid filament used in Subsection 4.2. The path orientations of specimens T_1 ($\alpha = 0$), T_2 ($\alpha = \pi/2$) and T_3 ($\alpha = \pm\pi/4$) with zigzag path and GCHP are adjusted to make them approximately parallel to the load orientations or the internal maximum principal stress orientations, and the thicknesses of the specimens are 2 *mm*, 2 *mm* and 15 *mm*, respectively. A 1 *mm/min* displacement load was applied by an electromechanical universal machine (10 *kN* capacity, Shenzhen Sans Testing Machine Co., Ltd.). All the test results are the medians of three replication experiments. As shown in Fig. 13(b), the ultimate failure forces of the contour path and CFS are almost equal because of their similar path orientations as those also happen in zigzag path and GCHP. Because the connection strength of filaments is lower than the filament strength per se, cracks of samples printed by contour parallel-based paths usually occur at the connection of adjacency paths. Additionally, the contour path and CFS generate severely underfilled gaps, which potentially exacerbate the stress concentration, thus ruducing the mechanical performance of the samples. On the other hand, because the gaps in the direction parallel paths are located at the areas near boundaries, which is not the critical position to influence mechanical properties. Consequently, the ultimate bearing capacities of samples printed by the zigzag path and GCHP are significantly higher than those of their counterparts printed by the contour path and CFS. The factors that affect the mechanical properties printed by extrusion-based additive manufacturing technology have been illustrated in detail in our previous works [11]. The mechanical performance of GCHP may not reach the peak because optimal path orientations can be strictly constructed by linking load conditions or internal stress orientations of the designing products. We leave this in our future work.

5. Conclusions

The path filling scheme is critical to fabrication quality of extrusion-based additive manufacturing. A novel globally continuous path filling scheme for connected geometries is proposed in this study. Compared with the prevailing continuous direction parallel paths, the process of geometric decomposition is not required in our scheme, and contours are connected to the interior paths to fulfill global continuity. In this case, the proposed scheme is applicable to more complicated geometries. Unlike filling gap functions in open-source software, our method to fill underfilled areas ensues path continuity. Curvature optimization saves printing time by alleviating velocity mutations incurred by sharp corners. With higher mechanical performance than CFS, the samples fabricated by the proposed path also exhibit better printing quality by reducing visible underfilled gaps. The novel path can implement partial infill. Although the applicability of the proposed method is demonstrated by fused filament fabrication, it is also applicable to wire and arc additive manufacturing. Especially for continuous filament fabrication, reduction and even elimination of fiber cutting will greatly simplify and accelerate the printing process.

Despite the remarkable benefits, the proposed scheme still exhibits some of the drawbacks of the traditional zigzag path. Compared with contour parallel paths, the proposed scheme is not suitable for thin-wall structures. Another shortcoming is that curvature optimization increases underfilled gaps near corners. In addition to the aforementioned deficiencies to be addressed or optimized in our future work, we will construct optimal path orientations of layers to further enhance the mechanical performance of products fabricated by the proposed path. This objective will be fulfilled by integrating topology optimization algorithm and our previous stress-base path.

Declaration of Competing Interest

None.

Acknowledgments

The paper is sponsored by the National Natural Science Foundation of China (grant numbers 52078181, 11802082 and 51878241).

References

[1] F. Wang, Z. Zhang, F. Ning, G. Wang, C. Dong, A mechanistic model for tensile property of continuous carbon fiber reinforced plastic composites built by fused filament fabrication, Addit. Manufact. 32 (2020), 101102, https://doi.org/10.1016/j.addma.2020.101102.
[2] M. Gomaa, W. Jabi, A.V. Reyes, V. Soebarto, 3D printing system for earth-based construction: case study of cob, Autom. Constr. 124 (3) (2021), 103577, https://doi.org/10.1016/j.autcon.2021.103577.
[3] T. Rayna, L. Striukova, From rapid prototyping to home fabrication: how 3D printing is changing business model innovation, Technol. Forecast. Soc. Chang. 102 (2016) 214–224, https://doi.org/10.1016/j.techfore.2015.07.023.
[4] P. Carneau, R. Mesnil, N. Roussel, O. Baverel, Additive manufacturing of cantilever-from masonry to concrete 3D printing, Autom. Constr. 116 (2020), 103184, https://doi.org/10.1016/j.autcon.2020.103184.
[5] S. Lin, Y.M. Xie, Q. Li, X. Huang, S. Zhou, On the shape transformation of cone scales, Soft Matter 12 (48) (2016) 9797–9802, https://doi.org/10.1039/C6SM01805J.
[6] S. Singh, S. Ramakrishna, R. Singh, Material issues in additive manufacturing: a review, J. Manuf. Process. 25 (2017) 185–200, https://doi.org/10.1016/j.jmapro.2016.11.006.
[7] S. He, C. Yan, Y. Deng, C.H. Lee, X. Zhou, A tolerance constrained G2 continuous path smoothing and interpolation method for industrial SCARA robots, Robot. Comput. Integr. Manuf. 63 (2020), 101907, https://doi.org/10.1016/j.rcim.2019.101907.
[8] J. Jiang, X. Xu, J. Stringer, Support structures for additive manufacturing: a review, J. Manufact. Mater. Process. 2 (4) (2018) 64, https://doi.org/10.3390/jmmp2040064.
[9] J. Jiang, J. Stringer, X. Xu, Support optimization for flat features via path planning in additive manufacturing, 3D Print. Addit. Manufact. 6 (3) (2019) 171–179, https://doi.org/10.1089/3dp.2017.0124.

[10] J.C. Steuben, A.P. Iliopoulos, J.G. Michopoulos, Implicit slicing for functionally tailored additive manufacturing, Comput. Aided Des. 77 (2016) 107–119, https://doi.org/10.1016/j.cad.2016.04.003.
[11] L. Xia, S. Lin, G. Ma, Stress-based tool-path planning methodology for fused filament fabrication, Addit. Manufact. 32 (2020), 101020, https://doi.org/10.1016/j.addma.2019.101020.
[12] Z. Lin, J. Fu, H. Shen, W. Gan, S. Yue, Tool path generation for multi-axis freeform surface finishing with the LKH TSP solver, Comput. Aided Des. 69 (2015) 51–61, https://doi.org/10.1016/j.cad.2015.07.002.
[13] S. Lin, L. Xia, G. Ma, S. Zhou, Y.M. Xie, A maze-like path generation scheme for fused deposition modeling, Int. J. Adv. Manuf. Technol. 104 (1) (2019) 1509–1519, https://doi.org/10.1007/s00170-019-03986-7.
[14] H. Yang, H. Shao, Distortion-oriented welding path optimization based on elastic net method and genetic algorithm, J. Mater. Process. Technol. 209 (9) (2009) 4407–4412, https://doi.org/10.1016/j.jmatprotec.2008.11.019.
[15] D. Ding, Z. Pan, D. Cuiuri, H. Li, A tool-path generation strategy for wire and arc additive manufacturing, Int. J. Adv. Manuf. Technol. 73 (1–4) (2014) 173–183, https://doi.org/10.1007/s00170-014-5808-5.
[16] N. Li, Y. Li, S. Liu, Rapid prototyping of continuous carbon fiber reinforced polylactic acid composites by 3D printing, J. Mater. Process. Technol. 238 (2016) 218–225, https://doi.org/10.1016/j.jmatprotec.2016.07.025.
[17] Y. Tu, Y. Tan, F. Zhang, J. Zhang, G. Ma, Shearing algorithm and device for the continuous carbon fiber 3D printing, J. Adv. Mech. Des. Syst. Manufact. 13 (1) (2019), https://doi.org/10.1299/jamdsm.2019jamdsm0016 pp. JAMDSM0016.
[18] W. Aiyiti, J. Xiang, L. Zhang, R. Chen, Study on the veritable parameters filling method of plasma arc welding based rapid prototyping, Key Eng. Mater. 522 (2012) 110–116, https://doi.org/10.4028/www.scientific.net/KEM.522.110.
[19] J. Jiang, Y. Ma, Path planning strategies to optimize accuracy, quality, build time and material use in additive manufacturing: a review, Micromachines 11 (7) (2020) 633, https://doi.org/10.3390/mi11070633.
[20] Y. Jin, Y. He, J. Fu, W. Gan, Z. Lin, Optimization of tool-path generation for material extrusion-based additive manufacturing technology, Addit. Manufact. 1 (2014) 32–47, https://doi.org/10.1016/j.addma.2014.08.004.
[21] G. Ma, Z. Li, L. Wang, G. Bai, Micro-cable reinforced geopolymer composite for extrusion-based 3D printing, Mater. Lett. 235 (2019) 144–147, https://doi.org/10.1016/j.matlet.2018.09.159.
[22] H. Zhao, F. Gu, Q. Huang, J. Garcia, Y. Chen, C. Tu, B. Benes, H. Zhang, D. Cohen-Or, B. Chen, Connected fermat spirals for layered fabrication, ACM Trans. Graph. 35 (4) (2016) 1–10, https://doi.org/10.1145/2897824.2925958.
[23] X. Zhai, F. Chen, Path planning of a type of porous structures for additive manufacturing, Comput. Aided Des. 115 (2019) 218–230, https://doi.org/10.1016/j.cad.2019.06.002.
[24] R. Dwivedi, R. Kovacevic, Automated torch path planning using polygon subdivision for solid freeform fabrication based on welding, J. Manuf. Syst. 23 (4) (2004) 278–291, https://doi.org/10.1016/S0278-6125(04)80040-2.
[25] G. Jin, W.D. Li, L. Gao, K. Popplewell, A hybrid and adaptive tool-path generation approach of rapid prototyping and manufacturing for biomedical models, Comput. Ind. 64 (3) (2013) 336–349, https://doi.org/10.1016/j.compind.2012.12.003.
[26] Y. Jin, Y. He, G. Fu, A. Zhang, J. Du, A non-retraction path planning approach for extrusion-based additive manufacturing, Robot. Comput. Integr. Manuf. 48 (2017) 132–144, https://doi.org/10.1016/j.rcim.2017.03.008.
[27] Y. Jin, Y. He, G. Xue, J. Fu, A parallel-based path generation method for fused deposition modeling, Int. J. Adv. Manuf. Technol. 77 (5–8) (2015) 927–937, https://doi.org/10.1007/s00170-014-6530-z.
[28] Y. Jin, J. Du, Z. Ma, A. Liu, Y. He, An optimization approach for path planning of high-quality and uniform additive manufacturing, Int. J. Adv. Manuf. Technol. 92 (1) (2017) 651–662, https://doi.org/10.1007/s00170-017-0207-3.
[29] D. Ding, Z. Pan, D. Cuiuri, H. Li, A practical path planning methodology for wire and arc additive manufacturing of thin-walled structures, Robot. Comput. Integr. Manuf. 34 (2015) 8–19, https://doi.org/10.1016/j.rcim.2015.01.003.
[30] J. Xu, L. Ding, L. Cai, L. Zhang, H. Luo, W. Qin, Volume-forming 3D concrete printing using a variable-size square nozzle, Autom. Constr. 104 (2019) 95–106, https://doi.org/10.1016/j.autcon.2019.03.008.
[31] Cura. https://ultimaker.com/software/ultimaker-cura, 2022 (Accessed date: 10 January 2022).
[32] Slic3r. https://slic3r.org/, 2022 (Accessed date: 10 January 2022).
[33] G. Jin, W. Li, C. Tsai, L. Wang, Adaptive tool-path generation of rapid prototyping for complex product models, J. Manuf. Syst. 30 (3) (2011) 154–164, https://doi.org/10.1016/j.jmsy.2011.05.007.
[34] G. Jin, W. Li, L. Gao, An adaptive process planning approach of rapid prototyping and manufacturing, Robot. Comput. Integr. Manuf. 29 (1) (2013) 23–38, https://doi.org/10.1016/j.rcim.2012.07.001.
[35] H. Giberti, L. Sbaglia, M. Urgo, A path planning algorithm for industrial processes under velocity constraints with an application to additive manufacturing, J. Manuf. Syst. 43 (2017) 160–167, https://doi.org/10.1016/j.jmsy.2017.03.003.
[36] An open-source library for geometry computational. https://ww2.mathworks.cn/help/matlab/elementary-polygons.html, 2022 (Accessed date: 10 January 2022).
[37] F. Luo, Y. Zhou, J. Yin, A universal velocity profile generation approach for high-speed machining of small line segments with look-ahead, Int. J. Adv. Manuf. Technol. 35 (5) (2007) 505–518, https://doi.org/10.1007/s00170-006-0735-8.